Published for SISSA by Springer

Received: March 30, 2021
Accepted: June 6, 2021
Published: June 30, 2021

JHEP06(2021)181

Amplitude analysis and branching-fraction measurement of $D_s^+ \to K_S^0\pi^+\pi^0$

BESIII

The BESIII collaboration

E-mail: besiii-publications@ihep.ac.cn

Abstract: By using 6.32 fb^{-1} of data collected with the BESIII detector at center-of-mass energies between 4.178 and 4.226 GeV, we perform an amplitude analysis of the decay $D_s^+ \to K_S^0\pi^+\pi^0$ and determine the relative fractions and phase differences of different intermediate processes, which include $K_S^0\rho(770)^+$, $K_S^0\rho(1450)^+$, $K^*(892)^0\pi^+$, $K^*(892)^+\pi^0$, and $K^*(1410)^0\pi^+$. With the detection efficiency based on the amplitude analysis results, the absolute branching fraction is measured to be $\mathcal{B}(D_s^+ \to K_S^0\pi^+\pi^0) = (5.43 \pm 0.30_{\rm stat} \pm 0.15_{\rm syst}) \times 10^{-3}$.

Keywords: Branching fraction, Charm physics, e^+-e^- Experiments

ArXiv ePrint: 2103.15098

https://doi.org/10.1007/JHEP06(2021)181

Contents

JHEP06(2021)181

1 Introduction

Knowledge of $D_s^\pm$ decay properties are vital input for studies of the B_s^0 hadron, whose decay channels are dominated by the final states involving $D_s^\pm$ mesons [1]. Furthermore, hadronic $D_s^\pm$ decays probe the interplay of short-distance weak-decay matrix elements and long-distance QCD interactions, and the measured branching fractions (BFs) provide valuable information concerning the amplitudes and phases that the strong force induces in the decay process [2–4]. The singly Cabibbo-suppressed (SCS) decay $D_s^+ \to K^0\pi^+\pi^0$ has a large BF of the order of 10^{-2} [1]. This decay, therefore, is often used as a reference channel for the other decays of $D_s^\pm$ mesons. Accurate knowledge of its substructure is essential to reduce the systematic uncertainties in those analyses using this channel. To date, there have been few measurements of charge-parity asymmetries $A_{\rm CP}$ in SCS $D_s^\pm$ decay modes in general [5, 6] and none for the mode discussed here.

An amplitude analysis of the D_s^+ decay to a three-body pseudoscalar meson final state is a powerful tool for studying the vector-pseudoscalar channels of the SCS D_s^+ decay. Table 1 shows the current measured values and theoretical predictions, in various models, for the BFs of $D_s^+ \to K_S^0\rho^+$, $K^*(892)^0\pi^+$, and $K^*(892)^+\pi^0$ (ρ^+ denotes $\rho(770)^+$ throughout this paper). References [7] and [8] took into account quark flavor SU(3) symmetry and its

Channel	PDG [1]	Y.L. Wu et al. [7]	H.Y. Cheng et al. [8]	F.S. Yu et al. [4]
$K^0\rho^+$	—	9.1 ± 7.7	11.47 ± 0.48	7.5 ± 2.1
$K^*(892)^0\pi^+$	2.13 ± 0.36	3.3 ± 3.5	3.65 ± 0.24	1.5 ± 0.7
$K^*(892)^+\pi^0$	—	1.3 ± 1.3	1.02 ± 0.07	0.1 ± 0.1

Table 1. Summary of D_s^+ decays to a vector and pseudoscalar meson, showing the measured BFs and theoretical predictions from various models ($\times 10^{-3}$).

breaking effects. Reference [4] used a generalized factorization method considering the resonance effects in the pole model for the annihilation contributions and introducing large strong phases between different topological diagrams. More precise experimental results are required to validate or falsify these theoretical predictions.

The CLEO collaboration has reported a measurement of $\mathcal{B}(D_s^+ \to K^0\pi^+\pi^0) = (1.00 \pm 0.18)\%$ [9], using 600 pb^{-1} of e^+e^- collisions recorded at a center-of-mass energy ($\sqrt{s}$) of 4.17 GeV. In this paper, by using 6.32 fb^{-1} of data collected with the BESIII detector at $\sqrt{s} = 4.178$-4.226 GeV, we perform the first amplitude analysis of $D_s^+ \to K_S^0\pi^+\pi^0$ and improve the measurement of its absolute BF.

2 Detector and data sets

The BESIII detector is a magnetic spectrometer [10, 11] located at the Beijing Electron Positron Collider (BEPCII) [12]. The cylindrical core of the BESIII detector consists of a helium-based multilayer drift chamber (MDC), a plastic scintillator time-of-flight system (TOF), and a CsI(Tl) electromagnetic calorimeter (EMC), which are all enclosed in a superconducting solenoidal magnet providing a 1.0 T magnetic field. The solenoid is supported by an octagonal flux-return yoke with resistive plate counter muon identifier modules interleaved with steel. The acceptance of charged particles and photons is 93% over a 4π solid angle. The charged-particle momenta resolution at 1.0 GeV/c is 0.5%, and the specific energy loss (dE/dx) resolution is 6% for the electrons from Bhabha scattering. The EMC measures photon energies with a resolution of 2.5% (5%) at 1 GeV in the barrel (end-cap) region. The time resolution of the TOF barrel part is 68 ps, while that of the end-cap part is 110 ps. The end-cap TOF was upgraded in 2015 with multi-gap resistive plate chamber technology, providing a time resolution of 60 ps [13–15].

The data samples used in this analysis are listed in table 2. For some aspects of the analysis, these samples are organized into three sample groups, 4.178 GeV, 4.189–4.219 GeV, and 4.226 GeV, that were acquired during the same year under consistent running conditions. Since the cross section of $D_s^{*\pm}D_s^{\mp}$ production in e^+e^- annihilation is about a factor of twenty larger than that of $D_s^+D_s^-$ [16], and the $D_s^{*\pm}$ meson decays to $\gamma D_s^{\pm}$ with a dominant BF of $(93.5 \pm 0.7)\%$ [1], the signal events discussed in this paper are selected from the process $e^+e^- \to D_s^{*\pm}D_s^{\mp} \to \gamma D_s^+ D_s^-$.

Simulated samples are produced with the GEANT4-based [17] Monte Carlo (MC) package, which includes the geometric description of the BESIII detector and the detector

JHEP06(2021)181

$\sqrt{s}$ (GeV)	$\mathcal{L}_{\rm int}$ (pb^{-1})	$M_{\rm rec}$ (GeV/c^2)
4.178	3189.0±0.2±31.9	[2.050, 2.180]
4.189	526.7±0.1±2.2	[2.048, 2.190]
4.199	526.0±0.1±2.1	[2.046, 2.200]
4.209	517.1±0.1±1.8	[2.044, 2.210]
4.219	514.6±0.1±1.8	[2.042, 2.220]
4.226	1047.3±0.1±10.2	[2.040, 2.220]

Table 2. The integrated luminosities ($\mathcal{L}_{\rm int}$) and the requirements on $M_{\rm rec}$ for various collision energies. The definition of $M_{\rm rec}$ is given in eq. (3.1). The first and second uncertainties are statistical and systematic, respectively.

response. These samples are used to determine the detection efficiency and to estimate the background. The simulation includes the beam-energy spread and initial-state radiation (ISR) in e^+e^- annihilations modeled with the generator KKMC [18]. The generic MC samples consist of the production of $D\bar{D}$ pairs with consideration of quantum coherence for all neutral D modes, the non-$D\bar{D}$ decays of the $\psi(3770)$, the ISR production of the J/ψ and $\psi(3686)$ states, and the continuum processes. The known decay modes are modeled with EVTGEN [19, 20] using the BFs taken from the Particle Data Group (PDG) [1], and the remaining unknown decays from the charmonium states with LUNDCHARM [21, 22]. Final-state radiation from charged particles is incorporated with the PHOTOS [23] package.

3 Event selection

The data samples were collected just above the $D_s^{*\pm}D_s^{\mp}$ threshold. The tag method allows clean signal samples to be selected, which provide an opportunity to perform amplitude analyses and to measure the absolute BFs of the hadronic D_s^+ meson decays. In the tag method, a single-tag (ST) candidate requires only one of the $D_s^{\pm}$ mesons to be reconstructed via a hadronic decay; a double-tag (DT) candidate has both $D_s^+D_s^-$ mesons reconstructed via hadronic decays. The DT candidates are required to have the D_s^+ meson decaying to the signal mode $D_s^+ \to K_S^0\pi^+\pi^0$ and the D_s^- meson decaying to a tag mode. (Charge conjugation is implied throughout this paper.) Nine tag modes are reconstructed and the corresponding mass windows on the tagging D_s^- mass ($M_{\rm tag}$) are listed in table 3. The $D_s^{\pm}$ candidates are constructed from individual $\pi^{\pm}$, $K^{\pm}$, η, η', K_S^0 and π^0 particles.

Charged track candidates from the MDC must satisfy $|\cos\theta| < 0.93$, where θ is the polar angle with respect to the direction of the positron beam. The closest approach to the interaction point is required to be less than 10 cm along the beam direction and less than 1 cm in the plane perpendicular to the beam. Particle identification (PID) of charged particles is implemented by combining the dE/dx information in the MDC and the time-of-flight information from the TOF system. For charged kaon (pion) candidates, the probability for the kaon (pion) hypothesis is required to be larger than that for the pion (kaon) hypothesis.

JHEP06(2021)181

Tag mode	Mass window (GeV/c^2)
$D_s^- \to K_S^0 K^-$	[1.948, 1.991]
$D_s^- \to K^+ K^- \pi^-$	[1.950, 1.986]
$D_s^- \to K_S^0 K^+ \pi^0$	[1.946, 1.987]
$D_s^- \to K^+ K^- \pi^- \pi^0$	[1.947, 1.982]
$D_s^- \to K_S^0 K^+ \pi^- \pi^-$	[1.953, 1.983]
$D_s^- \to \pi^- \pi^- \pi^+$	[1.952, 1.982]
$D_s^- \to \pi^- \eta_{\gamma\gamma}$	[1.930, 2.000]
$D_s^- \to \pi^- \pi^0 \eta_{\gamma\gamma}$	[1.920, 2.000]
$D_s^- \to \pi^- \eta'_{\pi^+\pi^-\eta_{\gamma\gamma}}$	[1.940, 1.996]

Table 3. Requirements on $M_{\rm tag}$ for various tag modes, where the η and η' subscripts denote the decay modes used to reconstruct these particles.

The K_S^0 mesons are reconstructed with pairs of two oppositely charged tracks, which satisfy $|\cos\theta| < 0.93$ and the distances of closest approach along the beam direction must be less than 20 cm. The decay length of the reconstructed K_S^0 in the signal side decay is required to be more than twice that of the vertex resolution away from the interaction point. The invariant masses of these charged track pairs are required to be in the range $[0.487, 0.511]\,{\rm GeV}/c^2$, which is about three times the resolution of the detector.

Photons are reconstructed from the clusters of deposited energy in the EMC. The shower time is required to be within $[0, 700]$ ns of the event start time in order to suppress electronics noise or e^+e^- beam background. Photon candidates within $|\cos\theta| < 0.80$ (barrel) are required to have an energy deposition larger than 25 MeV and those with $0.86 < |\cos\theta| < 0.92$ (end-cap) must have an energy deposition larger than 50 MeV. To suppress the noise from hadronic shower splitoffs, the calorimeter positions of photon candidates must lie outside a cone of 10° from all charged tracks. The π^0 (η) candidates are reconstructed through $\pi^0 \to \gamma\gamma$ ($\eta \to \gamma\gamma$) decays, with at least one barrel photon. The invariant mass of the photon pair for π^0 and η candidates must be in the ranges $[0.115, 0.150]\,{\rm GeV}/c^2$ and $[0.490, 0.580]\,{\rm GeV}/c^2$, respectively, which are about three times the resolution of the detector. A kinematic fit that constrains the $\gamma\gamma$ invariant mass to the π^0 or η nominal mass [1] is performed to improve the mass resolution. The χ^2 of the kinematic fit is required to be less than 30. The η' candidates are formed from the $\pi^+\pi^-\eta$ combinations with an invariant mass within a range of $[0.946, 0.970]\,{\rm GeV}/c^2$.

$D_s^\pm$ candidates with $M_{\rm rec}$ lying with the mass windows listed in table 2 are retained for further study. The quantity $M_{\rm rec}$ is defined as

$$M_{\rm rec} = \sqrt{\left(E_{\rm cm} - \sqrt{|\vec{p}_{D_s}|^2 + m_{D_s}^2}\right)^2 - |\vec{p}_{D_s}|^2}\,, \tag{3.1}$$

where $E_{\rm cm}$ is the initial energy of the e^+e^- center-of-mass system, $\vec{p}_{D_s}$ is the three-momentum of the $D_s^\pm$ candidate in the e^+e^- center-of-mass frame, and m_{D_s} is the $D_s^\pm$ nominal mass [1].

JHEP06(2021)181

A "$K^0_S K$" veto and a "D^0" veto are applied on the signal D_s^+ candidates. The Cabibbo-favored $D_s^+ \to K^0_S K^+$ decay contributes to the background when the K^+ is misidentified as a π^+. This background is reduced by a veto on the signal D_s^+ with $M_{K^0_S K^+} - m_{D_s} < -20\,\mathrm{MeV}/c^2$, where $M_{K^0_S K^+}$ is the invariant mass of the K^0_S and reconstructed π^+ track but assumed to be a kaon. There is also swap background where $D^0 \to K^0_S K^-\pi^+$ versus $\bar{D}^0 \to K^+\pi^-\pi^0$ fake $D_s^+ \to K^0_S\pi^+\pi^0$ versus $D_s^- \to K^+K^-\pi^-$ events through the exchange of K^0_S and K^+, or π^0 and K^-. Events which simultaneously satisfy $|M_{K^0_S K^-\pi^+} - m_{D^0}| < 30\,\mathrm{MeV}/c^2$ and $|M_{K^+\pi^-\pi^0} - m_{D^0}| < 30\,\mathrm{MeV}/c^2$ are rejected, where $M_{K^0_S K^-\pi^+}$ ($M_{K^+\pi^-\pi^0}$) is the invariant mass of the $K^0_S K^-\pi^+$ ($K^+\pi^-\pi^0$) combination and m_{D^0} is the D^0 nominal mass [1].

4 Amplitude analysis of $D_s^+ \to K^0_S\pi^+\pi^0$

4.1 Event selection

The following selection criteria are further applied in order to obtain data samples with high purities for the amplitude analysis. The selection criteria discussed in this section are not used in the BF measurement.

An eight-constraint kinematic fit is performed assuming the process $e^+e^- \to D_s^{*\pm}D_s^{\mp} \to \gamma D_s^+ D_s^-$, with D_s^- decaying to one of the tag modes and D_s^+ decaying to the signal mode. The combination with the minimum χ^2 is chosen, assuming that a D_s^{*+} meson decays to $D_s^+\gamma$ or a D_s^{*-} meson decays to $D_s^-\gamma$. In addition to the constraints of four-momentum conservation in the e^+e^- center-of-mass system, the invariant masses of $(\gamma\gamma)_{\pi^0}$, $(\pi^+\pi^-)_{K^0_S}$, tag D_s^-, and $D_s^{*\pm}$ candidates are constrained to the corresponding nominal masses [1]. In order to ensure that all candidates fall within the phase-space boundary, the constraint of the signal D_s^+ mass is added to the kinematic fit and the updated four-momenta are used for the amplitude analysis.

Moreover, it is required that the energy of the transition photon from $D_s^{*\pm} \to \gamma D_s^{\pm}$ is smaller than 0.18 GeV and the mass recoiling against this photon and the signal D_s^+ candidate lies within the range $[1.952, 1.995]\,\mathrm{GeV}/c^2$. Figure 1 shows the fits to the invariant-mass distributions of the accepted signal D_s^+ candidates, M_{sig}, for various data samples. The signal is described by an MC-simulated shape convolved with a Gaussian resolution function, and the background is described by a second-order Chebyshev function. Finally, a mass window, $[1.930, 1.990]\,\mathrm{GeV}/c^2$, is applied on the signal D_s^+ candidates. There are 352, 193, and 64 events retained for the amplitude analysis with purities, w_{sig}, of $(88.9 \pm 6.8)\%$, $(84.6 \pm 8.3)\%$, and $(75.9 \pm 14.3)\%$ for the data samples at $\sqrt{s} = 4.178$ GeV, 4.189–4.219 GeV, and 4.226 GeV, respectively.

4.2 Fit method

The intermediate-resonance composition in the decay $D_s^+ \to K^0_S\pi^+\pi^0$ is determined by an unbinned maximum-likelihood fit to data. The likelihood function is constructed with a probability density function (PDF), which depends on the momenta of the three daughter particles. The amplitude of the nth intermediate state (A_n) is

$$A_n = P_n S_n F_n^r F_n^D\,, \tag{4.1}$$

JHEP06(2021)181

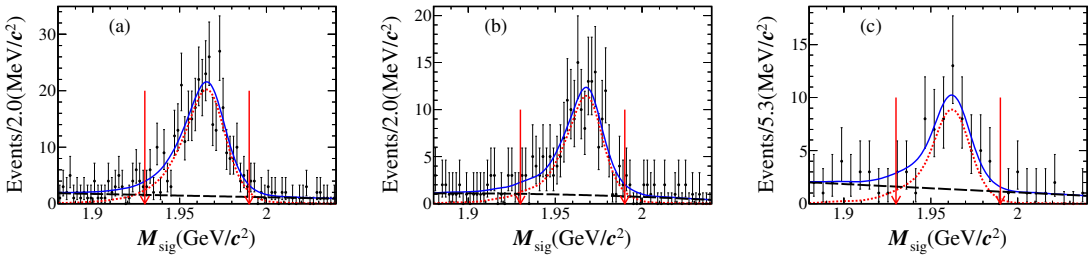

Figure 1. Fits to the $M_{\rm sig}$ distributions of the data samples at $\sqrt{s}$ = (a) 4.178 GeV, (b) 4.189–4.219 GeV, and (c) 4.226 GeV. The black points with error bars are data. The blue solid lines are the total fits. The red dotted and the black dashed lines are the fitted signal and background, respectively. The pairs of red arrows indicate the signal regions.

where S_n and $F_n^{r(D)}$ are the spin factor and the Blatt-Weisskopf barriers of the intermediate state (the $D_s^{\pm}$ meson), respectively, and P_n is the propagator of the intermediate resonance.

The total amplitude M is then the coherent sum of the amplitudes of intermediate processes, $M = \sum c_n A_n$, where $c_n = \rho_n e^{i\phi_n}$ is the corresponding complex coefficient. The magnitude ρ_n and phase ϕ_n are free parameters in the fit, and are defined relative to those of a reference mode, for which they are fixed. The signal PDF $f_S(p_j)$ is given by

$$f_S(p_j) = \frac{\epsilon(p_j)\,|M(p_j)|^2\,R_3(p_j)}{\int \epsilon(p_j)\,|M(p_j)|^2\,R_3(p_j)\,dp_j}\,, \tag{4.2}$$

where $\epsilon(p_j)$ is the detection efficiency parameterized in terms of the final four-momenta p_j. The index j refers to the different particles in the final states, and $R_3(p_j)$ is the standard element of three-body phase space. The normalization integral is determined by an MC integration,

$$\int \epsilon(p_j)\,|M(p_j)|^2\,R_3(p_j)\,dp_j \approx \frac{1}{N_M}\sum_k^{N_M}\frac{\left|M(p_j^k)\right|^2}{\left|M^g(p_j^k)\right|^2}\,, \tag{4.3}$$

where k is the index of the kth event and N_M is the number of the selected MC events. Here $M^g(p_j)$ is the PDF used to generate the MC samples in MC integration. To account for any bias caused by differences in PID and tracking efficiency between data and MC simulation, each signal MC event is weighted with a ratio, $\gamma_\epsilon(p)$, of the efficiency of data to that of MC simulation and the MC integration then becomes

$$\int \epsilon(p_j)\,|M(p_j)|^2\,R_3(p_j)\,dp_j \approx \frac{1}{N_M}\sum_k^{N_M}\frac{\left|M(p_j^k)\right|^2\gamma_\epsilon(p_j^k)}{\left|M^g(p_j^k)\right|^2}\,. \tag{4.4}$$

A signal-background combined PDF is introduced to account for the approximate 15% of background in this analysis. The background PDF is given by

$$f_B(p_j) = \frac{B(p_j)R_3(p_j)}{\int B(p_j)R_3(p_j)\,dp_j}\,. \tag{4.5}$$

JHEP06(2021)181

The background events in the signal region from the generic MC sample are used to model the corresponding background in data. The $M_{K^0_S\pi^+}$, $M_{K^0_S\pi^0}$, and $M_{\pi^+\pi^0}$ distributions of events outside the $M_{\rm sig}$ signal region between the data and the generic MC samples are compared to check validity of the background from the generic MC samples. The distributions of background events from the generic MC samples within and outside the $M_{\rm sig}$ signal region are also examined. They are found to be compatible within statistical uncertainties. The background shape $B(p_j)$ is derived using RooNDKeysPdf [24]. RooNDKeysPdf is a kernal estimation method [25] implemented in RooFit [24] which models the distribution of an input dataset as a superposition of Gaussian kernels. This background PDF is then added to the signal PDF incoherently and the combined PDF is written as

$$\begin{aligned} w_{\rm sig} f_S(p_j) + (1 - w_{\rm sig}) f_B(p_j) = w_{\rm sig} \frac{\epsilon(p_j)\,|M(p_j)|^2\,R_3(p_j)}{\int \epsilon(p_j)\,|M(p_j)|^2\,R_3(p_j)\,dp_j} \\ + (1 - w_{\rm sig}) \frac{B(p_j) R_3(p_j)}{\int B(p_j) R_3(p_j)\,dp_j}\,. \end{aligned} \tag{4.6}$$

A efficiency-corrected background shape, $B(p_j)_\epsilon \equiv B(p_j)/\epsilon(p_j)$ is introduced in order to factorize the $\epsilon(p_j)$ term out from the combined PDF. In this way, the $\epsilon(p_j)$ term, which is independent of the fitted variables, is regarded as a constant and can be dropped during the log-likelihood fit. As a consequence, the combined PDF becomes

$$\begin{aligned} w_{\rm sig} f_S(p_j) + (1 - w_{\rm sig}) f_B(p_j) = \epsilon(p_j) R_3(p_j) \left[\frac{w_{\rm sig}\,|M(p_j)|^2}{\int \epsilon(p_j)\,|M(p_j)|^2\,R_3(p_j)\,dp_j} \right. \\ \left. + \frac{(1 - w_{\rm sig}) B_\epsilon(p_j)}{\int \epsilon(p_j) B_\epsilon(p_j) R_3(p_j)\,dp_j} \right]. \end{aligned} \tag{4.7}$$

Next, the integration in the denominator of the background term can also be handled by the MC integration method in the same way as for the signal only sample:

$$\int \epsilon(p_j) B_\epsilon(p_j) R_3(p_j)\,dp_j \approx \frac{1}{N_M} \sum_k^{N_M} \frac{B_\epsilon(p_j^k)}{\left|M^g(p_j^k)\right|^2}\,. \tag{4.8}$$

Eventually, the log-likelihood is written as

$$\ln \mathcal{L} = \sum_{i=1}^{3} \sum_k^{N_{D,i}} \ln \left[w^i_{\rm sig} f_S(p_j^k) + (1 - w^i_{\rm sig}) f_B(p_j) \right], \tag{4.9}$$

where i indicate the data sample and N_D is the number of candidate events in data.

4.2.1 Blatt-Weisskopf barrier factors

For the process $a \to bc$, the Blatt-Weisskopf barrier $F_L(p_j)$ is parameterized as a function of the angular momenta L and the momenta q of the daughter b or c in the rest system of a,

$$\begin{aligned} F_{L=0}(q) &= 1, \\ F_{L=1}(q) &= \sqrt{\frac{z_0^2 + 1}{z^2 + 1}}, \\ F_{L=2}(q) &= \sqrt{\frac{z_0^4 + 3z_0^2 + 9}{z^4 + 3z^2 + 9}}, \end{aligned} \tag{4.10}$$

JHEP06(2021)181

where $z = qR$ and $z_0 = q_0 R$. The effective radius of the barrier R is fixed to $3.0\,\mathrm{GeV}^{-1}$ for the intermediate resonances and $5.0\,\mathrm{GeV}^{-1}$ for the D_s^+ meson.

4.2.2 Propagator

The intermediate resonances $K^*(892)^{0,+}$ and $K^*(1410)^0$ are parameterized as relativistic Breit-Wigner functions,

$$\begin{aligned} P &= \frac{1}{(m_0^2 - s_a) - i m_0 \Gamma(m)}\,, \\ \Gamma(m) &= \Gamma_0 \left(\frac{q}{q_0}\right)^{2L+1} \left(\frac{m_0}{m}\right) \left(\frac{F_L(q)}{F_L(q_0)}\right)^2\,, \end{aligned} \tag{4.11}$$

where s_a denotes the invariant-mass squared of the parent particle; m_0 and Γ_0 are the rest masses and the widths of the intermediate resonances, respectively, and are fixed to the PDG values [1].

We parameterize the ρ^+ and $\rho(1450)^+$ resonances by the Gounaris-Sakurai line-shape [26], which is given by

$$P_{\mathrm{GS}}(m) = \frac{1 + d\frac{\Gamma_0}{m_0}}{(m_0^2 - m^2) + f(m) - i m_0 \Gamma(m)}\,. \tag{4.12}$$

The function $f(m)$ is given by

$$f(m) = \Gamma_0 \frac{m_0^2}{q_0^3} \left[q^2 (h(m) - h(m_0)) + (m_0^2 - m^2) q_0^2 \left.\frac{dh}{d(m^2)}\right|_{m_0^2} \right]\,, \tag{4.13}$$

where

$$h(m) = \frac{2q}{\pi m} \ln\left(\frac{m + 2q}{2m_\pi}\right)\,, \tag{4.14}$$

and

$$\left.\frac{dh}{d(m^2)}\right|_{m_0^2} = h(m_0)\left[(8q_0^2)^{-1} - (2m_0^2)^{-1}\right] + (2\pi m_0^2)^{-1}\,. \tag{4.15}$$

The normalization condition at $P_{\mathrm{GS}}(0)$ fixes the parameter $d = f(0)/(\Gamma_0 m_0)$. It is found to be

$$d = \frac{3m_\pi^2}{\pi q_0^2} \ln\left(\frac{m_0 + 2q_0}{2m_\pi}\right) + \frac{m_0}{2\pi q_0} - \frac{m_\pi^2 m_0}{\pi q_0^3}\,. \tag{4.16}$$

4.2.3 Spin factors

The spin-projection operators are defined as [27]

$$\begin{aligned} P^{(1)}_{\mu\mu'}(a) &= -g_{\mu\mu'} + \frac{p_{a,\mu} p_{a,\mu'}}{p_a^2}\,, \\ P^{(2)}_{\mu\nu\mu'\nu'}(a) &= \frac{1}{2}\left(P^{(1)}_{\mu\mu'}(a) P^{(1)}_{\nu\nu'}(a) + P^{(1)}_{\mu\nu'}(a) P^{(1)}_{\nu\mu'}(a)\right) - \frac{1}{3} P^{(1)}_{\mu\nu}(a) P^{(1)}_{\mu'\nu'}(a)\,. \end{aligned} \tag{4.17}$$

The quantities p_a, p_b, and p_c are the momenta of particles a, b, and c, respectively, and $r_a = p_b - p_c$. The covariant tensors are given by

$$\begin{aligned} \tilde{t}^{(1)}_{\mu}(a) &= -P^{(1)}_{\mu\mu'}(a) r_a^{\mu'}\,, \\ \tilde{t}^{(2)}_{\mu\nu}(a) &= P^{(2)}_{\mu\nu\mu'\nu'}(a) r_a^{\mu'} r_a^{\nu'}\,. \end{aligned} \tag{4.18}$$

JHEP06(2021)181

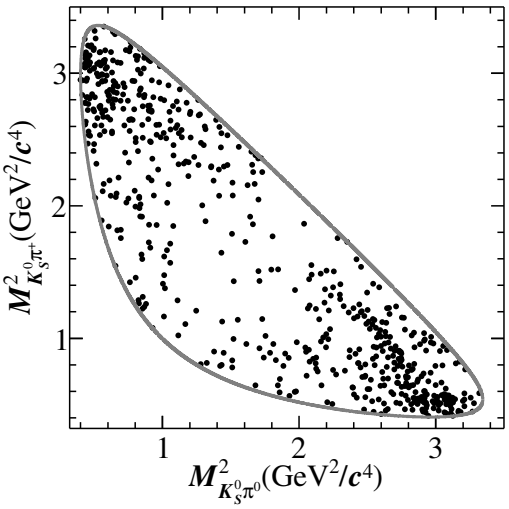

Figure 2. The Dalitz plot of the DT candidates from the data samples at $\sqrt{s} = 4.178$-$4.226\,\mathrm{GeV}$.

The spin factors for S, P, and D wave decays are

$$\begin{aligned} S &= 1\,, && (S \text{ wave}),\\ S &= \tilde{T}^{(1)\mu}(D_s^{\pm})\tilde{t}^{(1)}_{\mu}(a)\,, && (P \text{ wave}),\\ S &= \tilde{T}^{(2)\mu\nu}(D_s^{\pm})\tilde{t}^{(2)}_{\mu\nu}(a)\,, && (D \text{ wave}), \end{aligned} \tag{4.19}$$

where the $\tilde{T}^{(l)}$ factors have the same definition as $\tilde{t}^{(l)}$. The tensor describing the D_s^+ decay is denoted by $\tilde{T}$ and that of the a decay is denoted by $\tilde{t}$.

4.3 Fit results

The Dalitz plot of $M^2_{K^0_S\pi^0}$ versus $M^2_{K^0_S\pi^+}$ summed over all the data samples is shown in figure 2. One can see an anti-diagonal band corresponding to $K^0_S\rho^+$. In the fit, the magnitude and phase of the reference amplitude $D_s^+ \to K^0_S\rho^+$ are fixed to 1.0 and 0.0, respectively, while that of other amplitudes are floated. The masses and widths of all resonances are fixed to the corresponding PDG averages [1], and w^i_{sig} are fixed to the purities discussed in section 4.1. The systematic uncertainties associated with these fixed parameters will be considered by repeating the fit after variation of the tested ones. In addition to the dominating amplitude $D_s^+ \to K^0_S\rho^+$, we have tested for the contribution of all possible intermediate resonances including $K^*(892)^0$, $K^*(892)^+$, $K^*(1410)$, $K^*_0(1430)$, $K^*_2(1430)$, $\rho(1450)$, $K^*(1680)$, $\rho(1700)$, etc. We find that $D_s^+ \to K^0_S\rho(1450)^+$, $D_s^+ \to K^{*+}(892)\pi^0$, and $K^*(1410)^0\pi^+$ have a statistical significance greater than three standard deviations and retain these amplitudes in the final model.

The calculation of the fit fractions (FFs) for individual amplitudes, involves the phase-space MC truth information without detector acceptance or resolution effects. The FF for

JHEP06(2021)181

Amplitude	Magnitude (ρ_n)	Phase (ϕ_n)	FF (%)	Significance (σ)
$D_s^+ \to K_S^0\rho^+$	1.0(fixed)	0.0(fixed)	$50.2 \pm 7.2 \pm 3.9$	>10
$D_s^+ \to K_S^0\rho(1450)^+$	2.7 ± 0.5	$2.2 \pm 0.2 \pm 0.1$	$20.4 \pm 4.3 \pm 4.4$	>10
$D_s^+ \to K^*(892)^0\pi^+$	0.4 ± 0.1	$3.2 \pm 0.2 \pm 0.1$	$8.4 \pm 2.2 \pm 0.9$	5.0
$D_s^+ \to K^*(892)^+\pi^0$	0.3 ± 0.1	$0.2 \pm 0.2 \pm 0.2$	$4.6 \pm 1.4 \pm 0.4$	4.0
$D_s^+ \to K^*(1410)^0\pi^+$	0.8 ± 0.2	$0.2 \pm 0.3 \pm 0.1$	$3.3 \pm 1.6 \pm 0.5$	3.7

Table 4. Magnitudes, phases, FFs, and significances for the amplitudes. The uncertainties in the magnitudes are statistical only. The first and the second uncertainties in the phases and FFs are statistical and systematic, respectively. The total FF is 86.9%.

	B	C	D	E
A	20.3 ± 5.3	-4.1 ± 1.0	-2.6 ± 0.9	5.1 ± 1.6
B		-4.5 ± 0.9	-3.2 ± 0.7	0.8 ± 1.7
C			-0.5 ± 0.1	0.4 ± 1.0
D				0.5 ± 0.4

Table 5. Interference between amplitudes, in % of the total amplitude. A denotes $D_s^+ \to K_S^0\rho^+$, B $D_s^+ \to K_S^0\rho(1450)^+$, C $D_s^+ \to K^*(892)^0\pi^+$, D $D_s^+ \to K^*(892)^+\pi^0$, and E $D_s^+ \to K^*(1410)^0\pi^+$. The uncertainties are statistical only.

the nth amplitude is defined as

$$\mathrm{FF}_n = \frac{\sum^{N_{\mathrm{gen}}} |c_n A_n|^2}{\sum^{N_{\mathrm{gen}}} |M|^2}, \tag{4.20}$$

where N_{gen} is the number of phase-space MC events at generator level. These FFs will not sum to unity if there is net constructive or destructive interference. Interference IN between the nth and the n'th amplitudes is defined as (for $n < n'$ only)

$$\mathrm{IN}_{nn'} = \frac{\sum^{N_{\mathrm{gen}}} 2Re[c_n c_{n'}^* A_n A_{n'}^*]}{\sum^{N_{\mathrm{gen}}} |M|^2}. \tag{4.21}$$

In order to determine the statistical uncertainties of FFs, the amplitude coefficients are randomly sampled by a Gaussian-distributed amount set by the fit uncertainty and the covariance matrix. Then the distribution of each FF is fitted with a Gaussian function and the width of the Gaussian function is defined as the uncertainty of the FF.

The magnitudes, phases, FFs, and significances for the amplitudes are listed in table 4. The interference between amplitudes is listed in table 5. The Dalitz plot projections are shown in figure 3. The assignment of systematic uncertainties is discussed in next section.

4.4 Systematic uncertainties for amplitude analysis

The systematic uncertainties for the amplitude analysis are summarized in table 6, with their assignment described below.

i Resonance parameters. The masses and the widths of ρ^+, $\rho(1450)^+$, $K^*(892)^{0(+)}$, and $K^*(1410)^0$ are shifted by their corresponding uncertainties [1].

JHEP06(2021)181

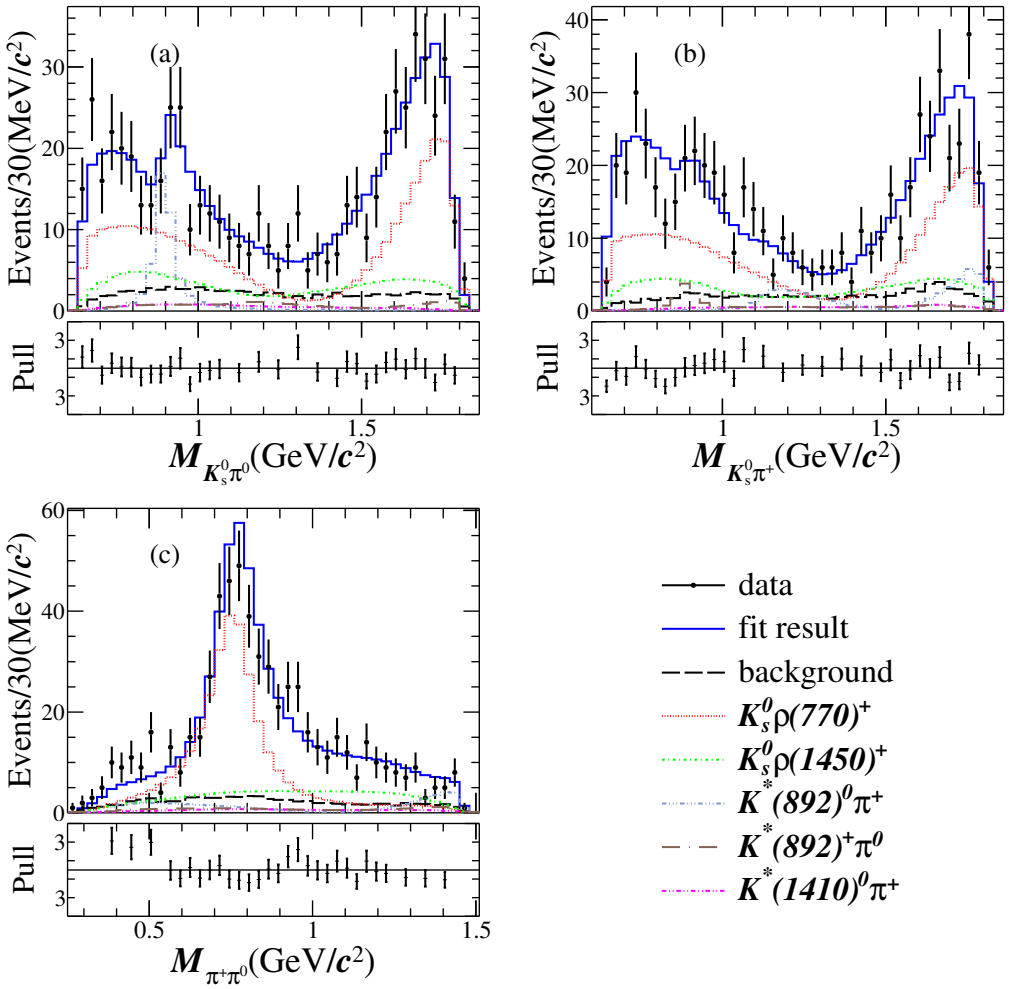

Figure 3. The projections of (a) $M_{K^0_S\pi^0}$, (b) $M_{K^0_S\pi^+}$, and (c) $M_{\pi^+\pi^0}$ from the nominal fit. The data samples at $\sqrt{s} = 4.178$-4.226 GeV are represented by points with error bars, the fit results by the solid blue lines, and the background estimated from generic MC samples by the black dashed lines. Colored curves show the components of the fit model. Due to interference effects, the total is not necessarily equal to the sum of the components. Pull projections are shown beneath each distribution, for which if there are less than 10 events in a certain bin, this bin is merged to the next bin until the number of events is larger than or equal to 10.

ii R values. The radii of the nonresonant state and $D_s^{\pm}$ mesons are varied within the range $[2.0, 4.0]\,\text{GeV}^{-1}$ for intermediate resonances and $[3.0, 7.0]\,\text{GeV}^{-1}$ for $D_s^{\pm}$ mesons.

iii Background estimation. The uncertainties associated with background are studied by varying the fractions of signal (equivalent to the fractions of background), i.e. w_{sig} in eq. (4.9). The fractions of signal for the three sample groups are varied by one corresponding statistical uncertainty. The largest differences from the nominal results are assigned as the uncertainties.

The other source of potential bias arisen from the knowledge of the background

JHEP06(2021)181

Amplitude		Source					
		i	ii	iii	iv	v	Total
$D_s^+ \to K_S^0\rho^+$	FF	0.03	0.49	0.02	0.23	0.03	0.54
$D_s^+ \to K_S^0\rho(1450)^+$	ϕ	0.34	0.38	0.15	0.16	0.06	0.56
	FF	0.34	0.95	0.05	0.19	0.03	1.03
$D_s^+ \to K^*(892)^0\pi^+$	ϕ	0.03	0.16	0.26	0.27	0.23	0.47
	FF	0.06	0.29	0.10	0.21	0.18	0.42
$D_s^+ \to K^*(892)^+\pi^0$	ϕ	0.03	0.33	0.70	0.21	0.06	0.80
	FF	0.10	0.03	0.15	0.25	0.03	0.31
$D_s^+ \to K^*(1410)^0\pi^+$	ϕ	0.15	0.02	0.25	0.14	0.06	0.33
	FF	0.14	0.22	0.13	0.09	0.03	0.31

Table 6. Systematic uncertainties on the ϕ and FFs for each amplitude in units of the corresponding statistical uncertainties. The sources are: (i) Fixed parameters in the amplitudes, (ii) The R values, (iii) Background, (iv) Experimental effects, (v) Fit bias.

distributions. We follow an alternative procedure by determining the background shape with another two variables, $M^2_{K^0_S\pi^+}$ versus $M^2_{\pi^+\pi^0}$, and change the smooth parameters in RooNDKeysPdf [24]. This resulting change in results is small enough to be ignored and so we assign no uncertainty from this source.

iv Experimental effects. To estimate the systematic uncertainty related to the difference in acceptance between MC and data associated with the PID and tracking efficiencies, that is γ_ϵ in eq. (4.4), the amplitude fit is performed varying the PID and tracking efficiencies according to their uncertainties.

v Fit bias. The amplitude analysis is performed on three-hundred data-sized signal MC samples and the pulls, which are the normalized-residual distributions of the fit, are inspected to look for biases or significant excursions from a normal distribution. These studies indicate that the FFs of $D_s^+ \to K^*(892)^0\pi^+$ and $D_s^+ \to K^*(1410)^0\pi^+$ are slightly biased. Therefore, we correct the biased FFs by the mean values of the pull distributions (from 8.9% to 8.4% for $D_s^+ \to K^*(892)^0\pi^+$ and from 3.5% to 3.3% for $D_s^+ \to K^*(1410)^0\pi^+$.) In addition, the statistical uncertainties of the FF and phase of $D_s^+ \to K^*(892)^0\pi^+$ are overestimated. We scale the uncertainties by the widths of the pulls (a factor of 0.84 for the FF and 0.85 for the phase). The systematic uncertainty of fit bias is assigned as the statistical uncertainty of the mean value. An additional systematic uncertainty due to the scale is taken into account by $\sqrt{2f\Delta f}$, where f is the fitted width and Δf is its uncertainty [28, 29].

JHEP06(2021)181

Tag mode	(I) $N_{\rm ST}$	(II) $N_{\rm ST}$	(III) $N_{\rm ST}$
$D_s^- \to K_S^0 K^-$	31668 ± 315	18340 ± 260	6550 ± 158
$D_s^- \to K^+ K^- \pi^-$	135867 ± 610	80417 ± 507	28289 ± 328
$D_s^- \to K_S^0 K^- \pi^0$	11284 ± 512	6729 ± 462	2144 ± 218
$D_s^- \to K^+ K^- \pi^- \pi^0$	38421 ± 767	22894 ± 645	7855 ± 439
$D_s^- \to K_S^0 K^+ \pi^- \pi^-$	15644 ± 289	8922 ± 229	3241 ± 169
$D_s^- \to \pi^- \pi^- \pi^+$	37702 ± 853	21675 ± 772	7506 ± 392
$D_s^- \to \pi^- \eta_{\gamma\gamma}$	18070 ± 560	10033 ± 355	3699 ± 244
$D_s^- \to \pi^- \pi^0 \eta_{\gamma\gamma}$	40862 ± 1313	25877 ± 1823	10659 ± 1060
$D_s^- \to \pi^- \eta'_{\pi^+\pi^-\eta_{\gamma\gamma}}$	7773 ± 143	4464 ± 111	1676 ± 74

Table 7. The ST yields for the samples collected at $\sqrt{s}$ = (I) 4.178 GeV, (II) 4.199–4.219 GeV, and (III) 4.226 GeV. The uncertainties are statistical.

5 Branching fraction measurement of $D_s^+ \to K_S^0 \pi^+ \pi^0$

With the selection criteria described in section 3, the best tag candidate with $M_{\rm rec}$ closest to the $D_s^\pm$ nominal mass [1] is chosen if there are multiple ST candidates. The yields for various tag modes are listed in table 7 and obtained by fitting the corresponding $M_{\rm tag}$ distributions. As an example, the fits to the data sample at $\sqrt{s} = 4.178$ GeV are shown in figure 4. In the fits, the signal is modeled by an MC-simulated shape convolved with a Gaussian function to take into account the data-MC resolution difference. The background is described by a second-order Chebyshev function. MC studies show that there is no significant peaking background in any tag mode, except for $D^- \to K_S^0 \pi^-$ and $D_s^- \to \eta \pi^+ \pi^- \pi^-$ faking the $D_s^- \to K_S^0 K^-$ and $D_s^- \to \pi^- \eta'$ tags, respectively. Therefore, the MC-simulated shapes of these two peaking background sources are added to the background polynomial functions.

Once a tag mode is identified, we search for the signal decay $D_s^+ \to K_S^0 \pi^+ \pi^0$. In the case of multiple candidates, the DT candidate with the average mass, $(M_{\rm sig} + M_{\rm tag})/2$, closest to the $D_s^\pm$ nominal mass is retained.

To measure the BF, we start from the following equations for a single tag mode:

$$N_{\rm tag}^{\rm ST} = 2 N_{D_s^+ D_s^-} \mathcal{B}_{\rm tag} \epsilon_{\rm tag}^{\rm ST} , \tag{5.1}$$

$$N_{\rm tag,sig}^{\rm DT} = 2 N_{D_s^+ D_s^-} \mathcal{B}_{\rm tag} \mathcal{B}_{\rm sig} \epsilon_{\rm tag,sig}^{\rm DT} , \tag{5.2}$$

where $N_{D_s^+ D_s^-}$ is the total number of $D_s^{*\pm} D_s^\mp$ pairs produced from the e^+e^- collisions; $N_{\rm tag}^{\rm ST}$ is the ST yield for the tag mode; $N_{\rm tag,sig}^{\rm DT}$ is the DT yield; $\mathcal{B}_{\rm tag}$ and $\mathcal{B}_{\rm sig}$ are the BFs of the tag and signal modes, respectively; $\epsilon_{\rm tag}^{\rm ST}$ is the ST efficiency to reconstruct the tag mode; and $\epsilon_{\rm tag,sig}^{\rm DT}$ is the DT efficiency to reconstruct both the tag and the signal decay modes. In the case of more than one tag modes and sample groups,

$$N_{\rm total}^{\rm DT} = \Sigma_{\alpha,i} N_{\alpha,{\rm sig},i}^{\rm DT} = \mathcal{B}_{\rm sig} \Sigma_{\alpha,i} 2 N_{D_s^+ D_s^-} \mathcal{B}_\alpha \epsilon_{\alpha,{\rm sig},i}^{\rm DT} , \tag{5.3}$$

JHEP06(2021)181

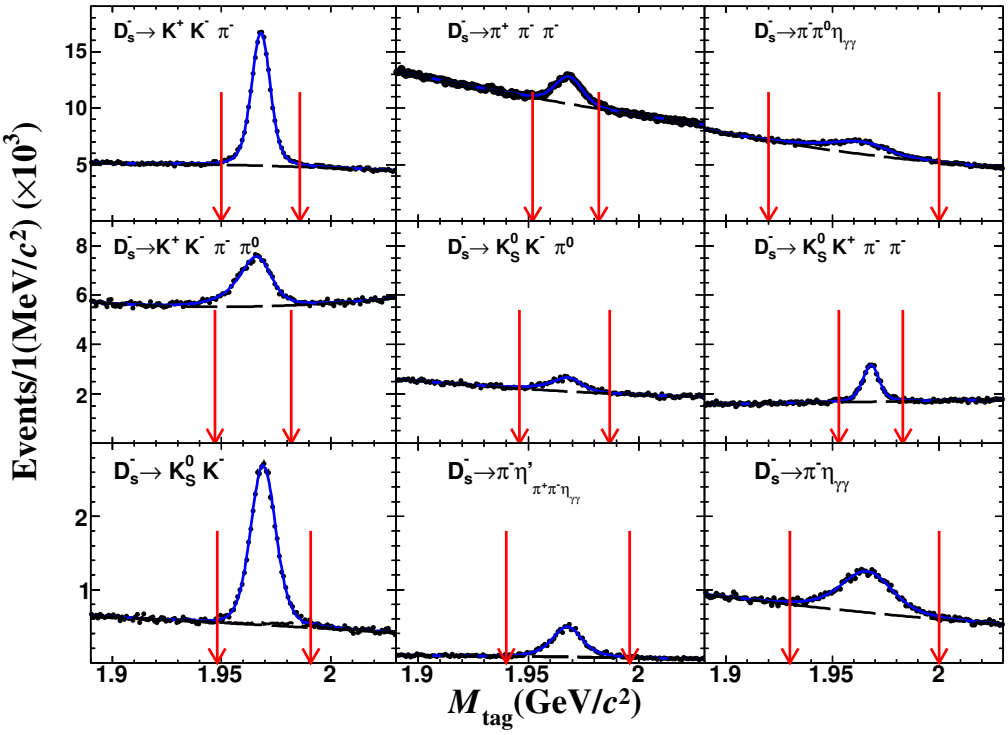

Figure 4. Fits to the $M_{\rm tag}$ distributions of the ST candidates from the data sample at $\sqrt{s} = 4.178\,\text{GeV}$. The points with error bars are data, the blue solid lines are the total fits, and the black dashed lines are background. The pairs of red arrows denote the signal regions.

where α represents tag modes in the ith sample group. By isolating $\mathcal{B}_{\rm sig}$, we find

$$\mathcal{B}_{\rm sig} = \frac{N^{\rm DT}_{\rm total}}{\mathcal{B}_{K^0_S\to\pi^+\pi^-}\mathcal{B}_{\pi^0\to\gamma\gamma}\sum_{\alpha,i} N^{\rm ST}_{\alpha,i}\epsilon^{\rm DT}_{\alpha,{\rm sig},i}/\epsilon^{\rm ST}_{\alpha,i}}\,, \tag{5.4}$$

where $N^{\rm ST}_{\alpha,i}$ and $\epsilon^{\rm ST}_{\alpha,i}$ are obtained from the data and generic MC samples, respectively, while $\epsilon^{\rm DT}_{\alpha,{\rm sig},i}$ is determined with signal MC samples, where $D_s^+ \to K^0_S\pi^+\pi^0$ events are generated according to the results of the amplitude analysis. The two branching ratios $\mathcal{B}_{K^0_S\to\pi^+\pi^-}$ and $\mathcal{B}_{\pi^0\to\gamma\gamma}$ have been introduced to account for the fact that the signal is reconstructed through these decays.

The DT yield $N^{\rm DT}_{\rm total}$ is found to be 666 ± 37 from the fit to the $M_{\rm sig}$ distribution of the selected $D_s^+ \to K^0_S\pi^+\pi^0$ candidates. The fit result is shown in figure 5. The signal shape is described by an MC-simulated shape convolved with a Gaussian function to take into account the data-MC resolution difference. The background shape is described by an MC-simulated shape, which includes the small peaking background (2.1%) that is mainly from $D_s^+ \to \pi^+\pi^+\pi^-\pi^0$ decays. The width of the Gaussian function is fixed to be $1.9 \pm 1.1\,\text{MeV}/c^2$, which is extracted from the control sample of $D_s^+ \to K^0_S K^+\pi^0$ decays. Note that the DT yield is larger than the fit yields of figure 1 since the kinematic fit and selections discussed in section 4.1 is not applied in the BF measurement.

JHEP06(2021)181

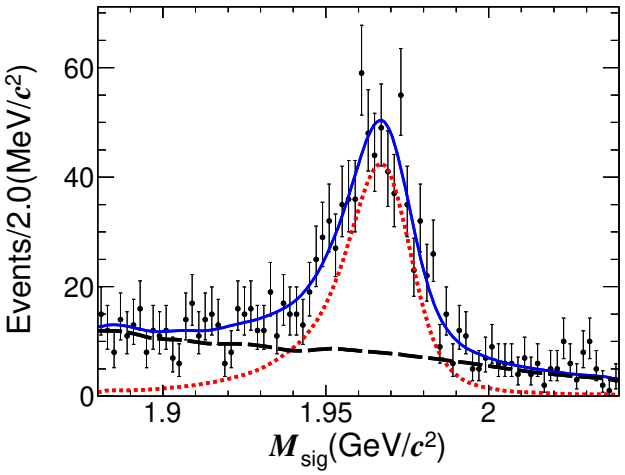

Figure 5. Fit to the $M_{\rm sig}$ distribution of the DT candidates from the data samples at $\sqrt{s} = 4.178$-4.226 GeV. The data are represented by points with error bars, the total fit by the blue solid line, and the fitted signal and the fitted background by the red dotted and the black dashed lines, respectively.

We take the differences in pion tracking efficiency between data and MC simulation into account, and apply a correction to the MC signal efficiency of +0.3%. The differences in PID efficiency are negligible. The BF is determined to be $\mathcal{B}(D_s^+ \to K_S^0\pi^+\pi^0) = (5.43 \pm 0.30_{\rm stat} \pm 0.15_{\rm syst}) \times 10^{-3}$.

In order to test CP conservation in the decay, the BFs are measured separately for the charge-conjugated modes. The BFs of $D_s^+ \to K_S^0\pi^+\pi^0$ and $D_s^- \to K_S^0\pi^-\pi^0$ are measured to be $(5.33 \pm 0.41_{\rm stat} \pm 0.15_{\rm syst}) \times 10^{-3}$ and $(5.63 \pm 0.44_{\rm stat} \pm 0.16_{\rm syst}) \times 10^{-3}$, respectively. The asymmetry of the BFs is determined to be $(2.7 \pm 5.5_{\rm stat} \pm 0.9_{\rm syst})\%$ by $A_{CP} = \frac{B(D_s^+) - B(D_s^-)}{B(D_s^+) + B(D_s^-)}$, where $B(D_s^{+(-)})$ is the BF of the decay $D_s^{+(-)} \to K_S^0\pi^{+(-)}\pi^0$. Hence, no CP violation is observed. Note that the systematic uncertainties related to K_S^0 and π^0 reconstructions cancel in the A_{CP} calculation.

The following sources of the systematic uncertainties are taken into account for the BF measurement.

- Signal shape. The systematic uncertainty due to the signal shape is studied by repeating the fit with an alternative width of the convolved Gaussian. This width is varied according to the uncertainty of the control sample.

- Background shape. Since $q\bar{q}$ or non-$D_s^{*\pm}D_s^{\mp}$ open charm are the major background sources, we alter the MC shapes by varying the relative fractions of the background from $q\bar{q}$ or non-$D_s^{*+}D_s^-$ open charm by $\pm 30\%$. This 30% is the statistical uncertainties of the cross section of $q\bar{q}$ and non-$D_s^{*+}D_s^-$ open charm in the data sample. The largest change is taken as the corresponding systematic uncertainty.

- π^+ tracking/PID efficiency. The π^+ tracking and PID efficiencies are studied with $e^+e^- \to K^+K^-\pi^+\pi^-$ events. The data-MC efficiency ratios of the π^+ tracking and

JHEP06(2021)181

PID efficiencies are 1.003 ± 0.002 and 1.000 ± 0.002, respectively. After multiplying the signal efficiencies by the factor 1.003, we assign 0.2% and 0.2% as the systematic uncertainties arising from π^+ PID and tracking, respectively.

- K^0_S reconstruction. The systematic uncertainty related to the K^0_S reconstruction efficiency is estimated with the control samples of $J/\psi \to K^*(892)^\mp K^\pm$ and $J/\psi \to \phi K^0_S K^\pm \pi^\mp$. Selection criteria mentioned in section 3 are used to reconstruct all the particles in the event except K^0_S. The number of K^0_Ss is determined by fitting the distribution of missing mass squared. By applying K^0_S selection, the number of reconstructed K^0_S is determined. The associated systematic uncertainty is assigned as 1.5% per K^0_S according to the efficiency difference of data and MC samples.

- π^0 reconstruction. The systematic uncertainty of the π^0 reconstruction efficiency is investigated by using a control sample of the process $e^+e^- \to K^+K^-\pi^+\pi^-\pi^0$. Selection criteria mentioned in section 3 are used to reconstruct the two kaons and the two pions. The recoiling mass distribution of $K^+K^-\pi^+\pi^-$ is fitted to obtain the total number of π^0s and the π^0 selection is applied to determined the number of reconstructed π^0s. The efficiency difference of data and MC samples is then determined to be 2.0% per π^0.

- MC statistics. The uncertainty due to the limited MC statistics is obtained by $\sqrt{\sum_i (f_i \frac{\delta_{\epsilon_i}}{\epsilon_i})^2}$, where f_i is the tag yield fraction, and ϵ_i and δ_{ϵ_i} are the signal efficiency and the corresponding uncertainty of tag mode i, respectively.

- Dalitz model. The uncertainty from the Dalitz model is estimated by varying the Dalitz model parameters based on their error matrix. The distribution of 600 efficiencies resulting from this variation is fitted by a Gaussian function and the fitted width divided by the mean value is taken as an uncertainty.

- Peaking background. A sample of $D^+_s \to \pi^+\pi^+\pi^-\pi^0$ is reconstructed with the same tag modes and selection criteria as the nominal analysis except the K^0_S selection is replaced by a K^0_S veto on the $\pi^+\pi^-$ invariant mass to remove events from $D^+_s \to K^0_S\pi^+\pi^0$. The background contributed by the decay $D^+_s \to \pi^+\pi^+\pi^-\pi^0$ is then estimated to be 2.1% of the $D^+_s \to K^0_S\pi^+\pi^0$ signal events. The relative uncertainty of this background is conservatively estimated to be 8% and corresponds to about one event in the $D^+_s \to K^0_S\pi^+\pi^0$ decay. Therefore, the associated uncertainty in the BF measurement is 0.2%.

All of the systematic uncertainties are summarized in table 8. Adding them in quadrature gives a total systematic uncertainty in the BF measurement of 2.8%.

6 Summary

An amplitude analysis has been performed for the decay $D^+_s \to K^0_S\pi^+\pi^0$. The results for the FFs and phases among the different intermediate processes are listed in table 4. After

JHEP06(2021)181

Source	Sys. Uncertainty (%)
Signal shape	0.8
Background shape	0.5
π^+ PID efficiency	0.2
π^+ tracking efficiency	0.2
K^0_S reconstruction	1.5
π^0 reconstruction	2.0
MC statistics	0.3
Dalitz model	0.8
Peaking Background	0.2
Total	2.8

Table 8. Systematic uncertainties in the BF measurement.

calculating a detection efficiency that accounts for the variation of decays over phase space found in the amplitude analysis, the BF for the decay $D_s^+ \to K^0_S\pi^+\pi^0$ is measured to be $(5.43 \pm 0.30_{\rm stat} \pm 0.15_{\rm syst}) \times 10^{-3}$ with an improved precision by about a factor of 3 compared to the PDG value [1]. The BFs for the intermediate processes are calculated with $\mathcal{B}_i = {\rm FF}_i \times \mathcal{B}(D_s^+ \to K^0_S\pi^+\pi^0)$ and listed in table 9. Assuming $\mathcal{B}(K^0 \to K^0_S) = 0.5$, we determine $\mathcal{B}(D_s^+ \to K^0\rho^+) = (5.46 \pm 0.84_{\rm stat} \pm 0.44_{\rm syst}) \times 10^{-3}$, $\mathcal{B}(D_s^+ \to K^*(892)^0\pi^+) = (2.71 \pm 0.72_{\rm stat} \pm 0.30_{\rm syst}) \times 10^{-3}$, and $\mathcal{B}(D_s^+ \to K^*(892)^+\pi^0) = (0.75 \pm 0.24_{\rm stat} \pm 0.06_{\rm syst}) \times 10^{-3}$. Our results are valuable for a deeper understanding of quark flavor SU(3) symmetry, SU(3) breaking effects, and other related theoretical issues.

These results can be compared to the current theoretical predictions [4, 7, 8]. The predictions in ref. [7] are consistent with our results, but their large uncertainties make the comparisons less conclusive. The calculations in ref. [8] have small uncertainties, while the predicted $\mathcal{B}(D_s^+ \to K^0\rho^+)$ is over five standard deviations off the measured one. The predictions in ref. [4] have moderate uncertainties and match our measurements in principle, but the predicted $\mathcal{B}(D_s^+ \to K^*(892)^+\pi^0)$ is only marginally consistent with our measurement. Based on the current experimental and theoretical precisions, it is difficult to draw a definite conclusion to discriminate between models yet.

The asymmetry for the BFs of the decays $D_s^+ \to K^0_S\pi^+\pi^0$ and $D_s^- \to K^0_S\pi^-\pi^0$ is determined to be $(2.7 \pm 5.5_{\rm stat} \pm 0.9_{\rm syst})\%$. No evidence for CP violation is found.

Acknowledgments

The BESIII collaboration thanks the staff of BEPCII and the IHEP computing center for their strong support. This work is supported in part by National Key Research and Development Program of China under Contracts Nos. 2020YFA0406400, 2020YFA0406300; National Natural Science Foundation of China (NSFC) under Contracts Nos. 11625523, 11635010, 11735014, 11775027, 11822506, 11835012, 11875054, 11935015, 11935016, 11935018, 11961141012; the Chinese Academy of Sciences (CAS) Large-Scale Scientific Facility Program; Joint Large-Scale Scientific Facility Funds of the NSFC and

JHEP06(2021)181

Intermediate process	BF (10^{-3})
$D_s^+ \to K_S^0\rho^+$	$2.73 \pm 0.42 \pm 0.22$
$D_s^+ \to K_S^0\rho(1450)^+$	$1.11 \pm 0.24 \pm 0.24$
$D_s^+ \to K^*(892)^0\pi^+$	$0.45 \pm 0.12 \pm 0.05$
$D_s^+ \to K^*(892)^+\pi^0$	$0.25 \pm 0.08 \pm 0.02$
$D_s^+ \to K^*(1410)^0\pi^+$	$0.18 \pm 0.09 \pm 0.03$

Table 9. The BFs for various intermediate processes with the final state $K_S^0\pi^+\pi^0$. The first and second uncertainties are statistical and systematic, respectively.

CAS under Contracts Nos. U2032104, U1732263, U1832207, U1932102; CAS Key Research Program of Frontier Sciences under Contracts Nos. QYZDJ-SSW-SLH003, QYZDJ-SSW-SLH040; 100 Talents Program of CAS; INPAC and Shanghai Key Laboratory for Particle Physics and Cosmology; ERC under Contract No. 758462; Technology Innovation Project of Shanxi Normal University No. 01053003; European Union Horizon 2020 research and innovation programme under Contract No. Marie Sklodowska-Curie grant agreement No 894790; German Research Foundation DFG under Contracts Nos. 443159800, Collaborative Research Center CRC 1044, FOR 2359, FOR 2359, GRK 214; Istituto Nazionale di Fisica Nucleare, Italy; Ministry of Development of Turkey under Contract No. DPT2006K-120470; National Science and Technology fund; Olle Engkvist Foundation under Contract No. 200-0605; STFC (United Kingdom); The Knut and Alice Wallenberg Foundation (Sweden) under Contract No. 2016.0157; The Royal Society, U.K. under Contracts Nos. DH140054, DH160214; The Swedish Research Council; U.S. Department of Energy under Contracts Nos. DE-FG02-05ER41374, DE-SC-0012069.

References

[1] Particle Data Group collaboration, *Review of Particle Physics*, *PTEP* **2020** (2020) 083C01 [INSPIRE].

[2] B. Bhattacharya and J.L. Rosner, *Decays of charmed mesons to PV final states*, *Phys. Rev. D* **79** (2009) 034016 [*Erratum ibid.* **81** (2010) 099903] [arXiv:0812.3167] [INSPIRE].

[3] H.-Y. Cheng and C.-W. Chiang, *Two-body hadronic charmed meson decays*, *Phys. Rev. D* **81** (2010) 074021 [arXiv:1001.0987] [INSPIRE].

[4] Y. Fu-Sheng, X.-X. Wang and C.-D. Lü, *Nonleptonic two-body decays of charmed mesons*, *Phys. Rev. D* **84** (2011) 074019 [arXiv:1101.4714] [INSPIRE].

[5] CLEO collaboration, *Improved measurement of absolute hadronic branching fractions of the D_s^+ meson*, *Phys. Rev. D* **88** (2013) 032009 [arXiv:1306.5363] [INSPIRE].

JHEP06(2021)181

[6] CLEO collaboration, *Measurements of d meson decays to two pseudoscalar mesons*, *Phys. Rev. D* **81** (2010) 052013 [arXiv:0906.3198] [INSPIRE].

[7] Y.-L. Wu, M. Zhong and Y.-F. Zhou, *Exploring final state hadron structure and* SU(3) *flavor symmetry breaking effects in* $D \to PP$ *and* $D \to PV$ *decays*, *Eur. Phys. J. C* **42** (2005) 391 [hep-ph/0405080] [INSPIRE].

[8] H.-Y. Cheng and C.-W. Chiang, *Revisiting CP-violation in* $D \to PP$ *and* VP *decays*, *Phys. Rev. D* **100** (2019) 093002 [arXiv:1909.03063] [INSPIRE].

[9] CLEO collaboration, *Measurement of the pseudoscalar decay constant* f_{D_s} *using* $D_s^+ \to \tau^+\nu$, $\tau^+ \to \rho^+\overline{\nu}$ *decays*, *Phys. Rev. D* **80** (2009) 112004 [arXiv:0910.3602] [INSPIRE].

[10] BESIII collaboration, *Design and construction of the BESIII detector*, *Nucl. Instrum. Meth. A* **614** (2010) 345 [arXiv:0911.4960] [INSPIRE].

[11] BESIII collaboration, *Future physics programme of BESIII*, *Chin. Phys. C* **44** (2020) 040001 [arXiv:1912.05983] [INSPIRE].

[12] C. Yu et al., *BEPCII Performance and Beam Dynamics Studies on Luminosity*, in *Proc. of International Particle Accelerator Conference (IPAC'16), Busan, Korea, May 8–13, 2016*, no. 7 in *International Particle Accelerator Conference*, Geneva, Switzerland, pp. 1014–1018, JACoW, June, 2016, DOI.

[13] X. Li et al., *Study of MRPC technology for BESIII endcap-TOF upgrade*, *Radiat. Detect. Technol. Methods* **1** (2017) 13.

[14] Y.-X. Guo et al., *The study of time calibration for upgraded end cap TOF of BESIII*, *Radiat. Detect. Technol. Methods* **1** (2017) 15.

[15] P. Cao et al., *Design and construction of the new BESIII endcap time-of-flight system with MRPC technology*, *Nucl. Instrum. Meth. A* **953** (2020) 163053.

[16] CLEO collaboration, *Measurement of charm production cross sections in* e^+e^- *annihilation at energies between 3.97 and 4.26 GeV*, *Phys. Rev. D* **80** (2009) 072001 [arXiv:0801.3418] [INSPIRE].

[17] GEANT4 collaboration, *GEANT4 — a simulation toolkit*, *Nucl. Instrum. Meth. A* **506** (2003) 250 [INSPIRE].

[18] S. Jadach, B.F.L. Ward and Z. Was, *Coherent exclusive exponentiation for precision Monte Carlo calculations*, *Phys. Rev. D* **63** (2001) 113009 [hep-ph/0006359] [INSPIRE].

[19] D.J. Lange, *The EvtGen particle decay simulation package*, *Nucl. Instrum. Meth. A* **462** (2001) 152 [INSPIRE].

[20] R.-G. Ping, *Event generators at BESIII*, *Chin. Phys. C* **32** (2008) 599 [INSPIRE].

[21] J.C. Chen, G.S. Huang, X.R. Qi, D.H. Zhang and Y.S. Zhu, *Event generator for* J/ψ *and* $\psi(2S)$ *decay*, *Phys. Rev. D* **62** (2000) 034003 [INSPIRE].

[22] R.-L. Yang, R.-G. Ping and H. Chen, *Tuning and validation of the Lundcharm model with* J/ψ *decays*, *Chin. Phys. Lett.* **31** (2014) 061301 [INSPIRE].

[23] E. Richter-Was, *QED bremsstrahlung in semileptonic B and leptonic* τ *decays*, *Phys. Lett. B* **303** (1993) 163 [INSPIRE].

[24] W. Verkerke and D.P. Kirkby, *RooFit Users Manual v2.07* (2006), https://doi.org/http://roofit.sourceforge.net.

JHEP06(2021)181

[25] K.S. Cranmer, *Kernel estimation in high-energy physics*, *Comput. Phys. Commun.* **136** (2001) 198 [hep-ex/0011057] [INSPIRE].

[26] G.J. Gounaris and J.J. Sakurai, *Finite-width corrections to the vector-meson-dominance prediction for* $\rho \to e^+e^-$, *Phys. Rev. Lett.* **21** (1968) 244 [INSPIRE].

[27] B.S. Zou and D.V. Bugg, *Covariant tensor formalism for partial-wave analyses of* ψ *decay to mesons*, *Eur. Phys. J. A* **16** (2003) 537 [hep-ph/0211457] [INSPIRE].

[28] R. Barlow, *Systematic Errors: facts and fictions*, in *Conference on Advanced Statistical Techniques in Particle Physics*, 7, 2002 [hep-ex/0207026] [INSPIRE].

[29] R.D. Cousins and V.L. Highland, *Incorporating systematic uncertainties into an upper limit*, *Nucl. Instrum. Meth. A* **320** (1992) 331 [INSPIRE].

JHEP06(2021)181

The BESIII collaboration

M. Ablikim[1], M.N. Achasov[10,b], P. Adlarson[67], S. Ahmed[15], M. Albrecht[4], R. Aliberti[28], A. Amoroso[66A,66C], M.R. An[32], Q. An[63,49], X.H. Bai[57], Y. Bai[48], O. Bakina[29], R. Baldini Ferroli[23A], I. Balossino[24A], Y. Ban[38,i], K. Begzsuren[26], N. Berger[28], M. Bertani[23A], D. Bettoni[24A], F. Bianchi[66A,66C], J. Bloms[60], A. Bortone[66A,66C], I. Boyko[29], R.A. Briere[5], H. Cai[68], X. Cai[1,49], A. Calcaterra[23A], G.F. Cao[1,54], N. Cao[1,54], S.A. Cetin[53A], J.F. Chang[1,49], W.L. Chang[1,54], G. Chelkov[29,a], D.Y. Chen[6], G. Chen[1], H.S. Chen[1,54], M.L. Chen[1,49], S.J. Chen[35], X.R. Chen[25], Y.B. Chen[1,49], Z. J Chen[20,j], W.S. Cheng[66C], G. Cibinetto[24A], F. Cossio[66C], X.F. Cui[36], H.L. Dai[1,49], X.C. Dai[1,54], A. Dbeyssi[15], R. E. de Boer[4], D. Dedovich[29], Z.Y. Deng[1], A. Denig[28], I. Denysenko[29], M. Destefanis[66A,66C], F. De Mori[66A,66C], Y. Ding[33], C. Dong[36], J. Dong[1,49], L.Y. Dong[1,54], M.Y. Dong[1,49,54], X. Dong[68], S.X. Du[71], Y.L. Fan[68], J. Fang[1,49], S.S. Fang[1,54], Y. Fang[1], R. Farinelli[24A], L. Fava[66B,66C], F. Feldbauer[4], G. Felici[23A], C.Q. Feng[63,49], J.H. Feng[50], M. Fritsch[4], C.D. Fu[1], Y. Gao[38,i], Y. Gao[64], Y. Gao[63,49], Y.G. Gao[6], I. Garzia[24A,24B], P.T. Ge[68], C. Geng[50], E.M. Gersabeck[58], A Gilman[61], K. Goetzen[11], L. Gong[33], W.X. Gong[1,49], W. Gradl[28], M. Greco[66A,66C], L.M. Gu[35], M.H. Gu[1,49], S. Gu[2], Y.T. Gu[13], C. Y Guan[1,54], A.Q. Guo[22], L.B. Guo[34], R.P. Guo[40], Y.P. Guo[9,g], A. Guskov[29,a], T.T. Han[41], W.Y. Han[32], X.Q. Hao[16], F.A. Harris[56], K.L. He[1,54], F.H. Heinsius[4], C.H. Heinz[28], T. Held[4], Y.K. Heng[1,49,54], C. Herold[51], M. Himmelreich[11,e], T. Holtmann[4], G.Y. Hou[1,54], Y.R. Hou[54], Z.L. Hou[1], H.M. Hu[1,54], J.F. Hu[47,k], T. Hu[1,49,54], Y. Hu[1], G.S. Huang[63,49], L.Q. Huang[64], X.T. Huang[41], Y.P. Huang[1], Z. Huang[38,i], T. Hussain[65], N Hüsken[22,28], W. Ikegami Andersson[67], W. Imoehl[22], M. Irshad[63,49], S. Jaeger[4], S. Janchiv[26], Q. Ji[1], Q.P. Ji[16], X.B. Ji[1,54], X.L. Ji[1,49], Y.Y. Ji[41], H.B. Jiang[41], X.S. Jiang[1,49,54], J.B. Jiao[41], Z. Jiao[18], S. Jin[35], Y. Jin[57], M.Q. Jing[1,54], T. Johansson[67], N. Kalantar-Nayestanaki[55], X.S. Kang[33], R. Kappert[55], M. Kavatsyuk[55], B.C. Ke[71,43], I.K. Keshk[4], A. Khoukaz[60], P. Kiese[28], R. Kiuchi[1], R. Kliemt[11], L. Koch[30], O.B. Kolcu[53A,d], B. Kopf[4], M. Kuemmel[4], M. Kuessner[4], A. Kupsc[67], M. G. Kurth[1,54], W. Kühn[30], J.J. Lane[58], J.S. Lange[30], P. Larin[15], A. Lavania[21], L. Lavezzi[66A,66C], Z.H. Lei[63,49], H. Leithoff[28], M. Lellmann[28], T. Lenz[28], C. Li[39], C.H. Li[32], Cheng Li[63,49], D.M. Li[71], F. Li[1,49], G. Li[1], H. Li[63,49], H. Li[43], H.B. Li[1,54], H.J. Li[16], J.L. Li[41], J.Q. Li[4], J.S. Li[50], Ke Li[1], L.K. Li[1], Lei Li[3], P.R. Li[31,l,m], S.Y. Li[52], W.D. Li[1,54], W.G. Li[1], X.H. Li[63,49], X.L. Li[41], Xiaoyu Li[1,54], Z.Y. Li[50], H. Liang[63,49], H. Liang[1,54], H. Liang[27], Y.F. Liang[45], Y.T. Liang[25], G.R. Liao[12], L.Z. Liao[1,54], J. Libby[21], C.X. Lin[50], B.J. Liu[1], C.X. Liu[1], D. Liu[63,49], F.H. Liu[44], Fang Liu[1], Feng Liu[6], H.B. Liu[13], H.M. Liu[1,54], Huanhuan Liu[1], Huihui Liu[17], J.B. Liu[63,49], J.L. Liu[64], J.Y. Liu[1,54], K. Liu[1], K.Y. Liu[33], L. Liu[63,49], M.H. Liu[9,g], P.L. Liu[1], Q. Liu[68], Q. Liu[54], S.B. Liu[63,49], Shuai Liu[46], T. Liu[1,54], W.M. Liu[63,49], X. Liu[31,l,m], Y. Liu[31,l,m], Y.B. Liu[36], Z.A. Liu[1,49,54], Z.Q. Liu[41], X.C. Lou[1,49,54], F.X. Lu[50], H.J. Lu[18], J.D. Lu[1,54], J.G. Lu[1,49], X.L. Lu[1], Y. Lu[1], Y.P. Lu[1,49], C.L. Luo[34], M.X. Luo[70], P.W. Luo[50], T. Luo[9,g], X.L. Luo[1,49], X.R. Lyu[54], F.C. Ma[33], H.L. Ma[1], L.L. Ma[41], M.M. Ma[1,54], Q.M. Ma[1], R.Q. Ma[1,54], R.T. Ma[54], X.X. Ma[1,54], X.Y. Ma[1,49], F.E. Maas[15], M. Maggiora[66A,66C], S. Maldaner[4], S. Malde[61], Q.A. Malik[65], A. Mangoni[23B], Y.J. Mao[38,i], Z.P. Mao[1], S. Marcello[66A,66C], Z.X. Meng[57], J.G. Messchendorp[55], G. Mezzadri[24A], T.J. Min[35], R.E. Mitchell[22], X.H. Mo[1,49,54], Y.J. Mo[6], N. Yu. Muchnoi[10,b], H. Muramatsu[59], S. Nakhoul[11,e], Y. Nefedov[29], F. Nerling[11,e], I.B. Nikolaev[10,b], Z. Ning[1,49], S. Nisar[8,h], S.L. Olsen[54], Q. Ouyang[1,49,54], S. Pacetti[23B,23C], X. Pan[9,g], Y. Pan[58], A. Pathak[1], A. Pathak[27], P. Patteri[23A], M. Pelizaeus[4], H.P. Peng[63,49], K. Peters[11,e], J. Pettersson[67], J.L. Ping[34], R.G. Ping[1,54], R. Poling[59], V. Prasad[63,49], H. Qi[63,49], H.R. Qi[52], K.H. Qi[25], M. Qi[35], T.Y. Qi[9], S. Qian[1,49], W.B. Qian[54], Z. Qian[50], C.F. Qiao[54], L.Q. Qin[12], X.P. Qin[9], X.S. Qin[41], Z.H. Qin[1,49], J.F. Qiu[1], S.Q. Qu[36], K.H. Rashid[65], K. Ravindran[21], C.F. Redmer[28], A. Rivetti[66C], V. Rodin[55], M. Rolo[66C], G. Rong[1,54], Ch. Rosner[15], M. Rump[60], H.S. Sang[63],

JHEP06(2021)181

A. Sarantsev[29,c], Y. Schelhaas[28], C. Schnier[4], K. Schoenning[67], M. Scodeggio[24A,24B], D.C. Shan[46], W. Shan[19], X.Y. Shan[63,49], J.F. Shangguan[46], M. Shao[63,49], C.P. Shen[9], H.F. Shen[1,54], P.X. Shen[36], X.Y. Shen[1,54], H.C. Shi[63,49], R.S. Shi[1,54], X. Shi[1,49], X. D Shi[63,49], J.J. Song[41], W.M. Song[27,1], Y.X. Song[38,i], S. Sosio[66A,66C], S. Spataro[66A,66C], K.X. Su[68], P.P. Su[46], F.F. Sui[41], G.X. Sun[1], H.K. Sun[1], J.F. Sun[16], L. Sun[68], S.S. Sun[1,54], T. Sun[1,54], W.Y. Sun[34], W.Y. Sun[27], X Sun[20,j], Y.J. Sun[63,49], Y.K. Sun[63,49], Y.Z. Sun[1], Z.T. Sun[1], Y.H. Tan[68], Y.X. Tan[63,49], C.J. Tang[45], G.Y. Tang[1], J. Tang[50], J.X. Teng[63,49], V. Thoren[67], W.H. Tian[43], Y.T. Tian[25], I. Uman[53B], B. Wang[1], C.W. Wang[35], D.Y. Wang[38,i], H.J. Wang[31,l,m], H.P. Wang[1,54], K. Wang[1,49], L.L. Wang[1], M. Wang[41], M.Z. Wang[38,i], Meng Wang[1,54], W. Wang[50], W.H. Wang[68], W.P. Wang[63,49], X. Wang[38,i], X.F. Wang[31,l,m], X.L. Wang[9,g], Y. Wang[50], Y. Wang[63,49], Y.D. Wang[37], Y.F. Wang[1,49,54], Y.Q. Wang[1], Y.Y. Wang[31,l,m], Z. Wang[1,49], Z.Y. Wang[1], Ziyi Wang[54], Zongyuan Wang[1,54], D.H. Wei[12], F. Weidner[60], S.P. Wen[1], D.J. White[58], U. Wiedner[4], G. Wilkinson[61], M. Wolke[67], L. Wollenberg[4], J.F. Wu[1,54], L.H. Wu[1], L.J. Wu[1,54], X. Wu[9,g], Z. Wu[1,49], L. Xia[63,49], H. Xiao[9,g], S.Y. Xiao[1], Z.J. Xiao[34], X.H. Xie[38,i], Y.G. Xie[1,49], Y.H. Xie[6], T.Y. Xing[1,54], G.F. Xu[1], Q.J. Xu[14], W. Xu[1,54], X.P. Xu[46], Y.C. Xu[54], F. Yan[9,g], L. Yan[9,g], W.B. Yan[63,49], W.C. Yan[71], Xu Yan[46], H.J. Yang[42,f], H.X. Yang[1], L. Yang[43], S.L. Yang[54], Y.X. Yang[12], Yifan Yang[1,54], Zhi Yang[25], M. Ye[1,49], M.H. Ye[7], J.H. Yin[1], Z.Y. You[50], B.X. Yu[1,49,54], C.X. Yu[36], G. Yu[1,54], J.S. Yu[20,j], T. Yu[64], C.Z. Yuan[1,54], L. Yuan[2], X.Q. Yuan[38,i], Y. Yuan[1], Z.Y. Yuan[50], C.X. Yue[32], A.A. Zafar[65], X. Zeng Zeng[6], Y. Zeng[20,j], A.Q. Zhang[1], B.X. Zhang[1], Guangyi Zhang[16], H. Zhang[63], H.H. Zhang[27], H.H. Zhang[50], H.Y. Zhang[1,49], J.J. Zhang[43], J.L. Zhang[69], J.Q. Zhang[34], J.W. Zhang[1,49,54], J.Y. Zhang[1], J.Z. Zhang[1,54], Jianyu Zhang[1,54], Jiawei Zhang[1,54], L.M. Zhang[52], L.Q. Zhang[50], Lei Zhang[35], S. Zhang[50], S.F. Zhang[35], Shulei Zhang[20,j], X.D. Zhang[37], X.Y. Zhang[41], Y. Zhang[61], Y. T. Zhang[71], Y.H. Zhang[1,49], Yan Zhang[63,49], Yao Zhang[1], Z.H. Zhang[6], Z.Y. Zhang[68], G. Zhao[1], J. Zhao[32], J.Y. Zhao[1,54], J.Z. Zhao[1,49], Lei Zhao[63,49], Ling Zhao[1], M.G. Zhao[36], Q. Zhao[1], S.J. Zhao[71], Y.B. Zhao[1,49], Y.X. Zhao[25], Z.G. Zhao[63,49], A. Zhemchugov[29,a], B. Zheng[64], J.P. Zheng[1,49], Y. Zheng[38,i], Y.H. Zheng[54], B. Zhong[34], C. Zhong[64], L.P. Zhou[1,54], Q. Zhou[1,54], X. Zhou[68], X.K. Zhou[54], X.R. Zhou[63,49], X.Y. Zhou[32], A.N. Zhu[1,54], J. Zhu[36], K. Zhu[1], K.J. Zhu[1,49,54], S.H. Zhu[62], T.J. Zhu[69], W.J. Zhu[9,g], W.J. Zhu[36], X.Y. Zhu[16], Y.C. Zhu[63,49], Z.A. Zhu[1,54], B.S. Zou[1], J.H. Zou[1]

[1] *Institute of High Energy Physics, Beijing 100049, People's Republic of China*
[2] *Beihang University, Beijing 100191, People's Republic of China*
[3] *Beijing Institute of Petrochemical Technology, Beijing 102617, People's Republic of China*
[4] *Bochum Ruhr-University, D-44780 Bochum, Germany*
[5] *Carnegie Mellon University, Pittsburgh, Pennsylvania 15213, U.S.A.*
[6] *Central China Normal University, Wuhan 430079, People's Republic of China*
[7] *China Center of Advanced Science and Technology, Beijing 100190, People's Republic of China*
[8] *COMSATS University Islamabad, Lahore Campus, Defence Road, Off Raiwind Road, 54000 Lahore, Pakistan*
[9] *Fudan University, Shanghai 200443, People's Republic of China*
[10] *G.I. Budker Institute of Nuclear Physics SB RAS (BINP), Novosibirsk 630090, Russia*
[11] *GSI Helmholtzcentre for Heavy Ion Research GmbH, D-64291 Darmstadt, Germany*
[12] *Guangxi Normal University, Guilin 541004, People's Republic of China*
[13] *Guangxi University, Nanning 530004, People's Republic of China*
[14] *Hangzhou Normal University, Hangzhou 310036, People's Republic of China*
[15] *Helmholtz Institute Mainz, Staudinger Weg 18, D-55099 Mainz, Germany*
[16] *Henan Normal University, Xinxiang 453007, People's Republic of China*
[17] *Henan University of Science and Technology, Luoyang 471003, People's Republic of China*
[18] *Huangshan College, Huangshan 245000, People's Republic of China*

JHEP06(2021)181

[19] Hunan Normal University, Changsha 410081, People's Republic of China
[20] Hunan University, Changsha 410082, People's Republic of China
[21] Indian Institute of Technology Madras, Chennai 600036, India
[22] Indiana University, Bloomington, Indiana 47405, U.S.A.
[23] INFN Laboratori Nazionali di Frascati, (A)INFN Laboratori Nazionali di Frascati, I-00044, Frascati, Italy; (B)INFN Sezione di Perugia, I-06100, Perugia, Italy; (C)University of Perugia, I-06100, Perugia, Italy
[24] INFN Sezione di Ferrara, (A)INFN Sezione di Ferrara, I-44122, Ferrara, Italy; (B)University of Ferrara, I-44122, Ferrara, Italy
[25] Institute of Modern Physics, Lanzhou 730000, People's Republic of China
[26] Institute of Physics and Technology, Peace Ave. 54B, Ulaanbaatar 13330, Mongolia
[27] Jilin University, Changchun 130012, People's Republic of China
[28] Johannes Gutenberg University of Mainz, Johann-Joachim-Becher-Weg 45, D-55099 Mainz, Germany
[29] Joint Institute for Nuclear Research, 141980 Dubna, Moscow region, Russia
[30] Justus-Liebig-Universitaet Giessen, II. Physikalisches Institut, Heinrich-Buff-Ring 16, D-35392 Giessen, Germany
[31] Lanzhou University, Lanzhou 730000, People's Republic of China
[32] Liaoning Normal University, Dalian 116029, People's Republic of China
[33] Liaoning University, Shenyang 110036, People's Republic of China
[34] Nanjing Normal University, Nanjing 210023, People's Republic of China
[35] Nanjing University, Nanjing 210093, People's Republic of China
[36] Nankai University, Tianjin 300071, People's Republic of China
[37] North China Electric Power University, Beijing 102206, People's Republic of China
[38] Peking University, Beijing 100871, People's Republic of China
[39] Qufu Normal University, Qufu 273165, People's Republic of China
[40] Shandong Normal University, Jinan 250014, People's Republic of China
[41] Shandong University, Jinan 250100, People's Republic of China
[42] Shanghai Jiao Tong University, Shanghai 200240, People's Republic of China
[43] Shanxi Normal University, Linfen 041004, People's Republic of China
[44] Shanxi University, Taiyuan 030006, People's Republic of China
[45] Sichuan University, Chengdu 610064, People's Republic of China
[46] Soochow University, Suzhou 215006, People's Republic of China
[47] South China Normal University, Guangzhou 510006, People's Republic of China
[48] Southeast University, Nanjing 211100, People's Republic of China
[49] State Key Laboratory of Particle Detection and Electronics, Beijing 100049, Hefei 230026, People's Republic of China
[50] Sun Yat-Sen University, Guangzhou 510275, People's Republic of China
[51] Suranaree University of Technology, University Avenue 111, Nakhon Ratchasima 30000, Thailand
[52] Tsinghua University, Beijing 100084, People's Republic of China
[53] Turkish Accelerator Center Particle Factory Group, (A)Istanbul Bilgi University, HEP Res. Cent., 34060 Eyup, Istanbul, Turkey; (B)Near East University, Nicosia, North Cyprus, Mersin 10, Turkey
[54] University of Chinese Academy of Sciences, Beijing 100049, People's Republic of China
[55] University of Groningen, NL-9747 AA Groningen, The Netherlands
[56] University of Hawaii, Honolulu, Hawaii 96822, U.S.A.
[57] University of Jinan, Jinan 250022, People's Republic of China
[58] University of Manchester, Oxford Road, Manchester, M13 9PL, United Kingdom
[59] University of Minnesota, Minneapolis, Minnesota 55455, U.S.A.
[60] University of Muenster, Wilhelm-Klemm-Str. 9, 48149 Muenster, Germany
[61] University of Oxford, Keble Rd, Oxford, U.K. OX13RH
[62] University of Science and Technology Liaoning, Anshan 114051, People's Republic of China
[63] University of Science and Technology of China, Hefei 230026, People's Republic of China

JHEP06(2021)181

[64] University of South China, Hengyang 421001, People's Republic of China
[65] University of the Punjab, Lahore-54590, Pakistan
[66] University of Turin and INFN, (A)University of Turin, I-10125, Turin, Italy; (B)University of Eastern Piedmont, I-15121, Alessandria, Italy; (C)INFN, I-10125, Turin, Italy
[67] Uppsala University, Box 516, SE-75120 Uppsala, Sweden
[68] Wuhan University, Wuhan 430072, People's Republic of China
[69] Xinyang Normal University, Xinyang 464000, People's Republic of China
[70] Zhejiang University, Hangzhou 310027, People's Republic of China
[71] Zhengzhou University, Zhengzhou 450001, People's Republic of China
[a] Also at the Moscow Institute of Physics and Technology, Moscow 141700, Russia
[b] Also at the Novosibirsk State University, Novosibirsk, 630090, Russia
[c] Also at the NRC "Kurchatov Institute", PNPI, 188300, Gatchina, Russia
[d] Currently at Istanbul Arel University, 34295 Istanbul, Turkey
[e] Also at Goethe University Frankfurt, 60323 Frankfurt am Main, Germany
[f] Also at Key Laboratory for Particle Physics, Astrophysics and Cosmology, Ministry of Education; Shanghai Key Laboratory for Particle Physics and Cosmology; Institute of Nuclear and Particle Physics, Shanghai 200240, People's Republic of China
[g] Also at Key Laboratory of Nuclear Physics and Ion-beam Application (MOE) and Institute of Modern Physics, Fudan University, Shanghai 200443, People's Republic of China
[h] Also at Harvard University, Department of Physics, Cambridge, MA, 02138, U.S.A.
[i] Also at State Key Laboratory of Nuclear Physics and Technology, Peking University, Beijing 100871, People's Republic of China
[j] Also at School of Physics and Electronics, Hunan University, Changsha 410082, China
[k] Also at Guangdong Provincial Key Laboratory of Nuclear Science, Institute of Quantum Matter, South China Normal University, Guangzhou 510006, China
[l] Also at Frontiers Science Center for Rare Isotopes, Lanzhou University, Lanzhou 730000, People's Republic of China
[m] Also at Lanzhou Center for Theoretical Physics, Lanzhou University, Lanzhou 730000, People's Republic of China

JHEP06(2021)181